Contents lists available at ScienceDirect

Journal of Alloys and Compounds

journal homepage: http://ees.elsevier.com

Improved pseudocapacitances of supercapacitors based on electrodes of nitrogen-doped $Ti_3C_2T_x$ nanosheets with in-situ growth of carbon nanotubes

Yi Sun [a,b], Ruowei Yi [c,d], Yinchao Zhao [e], Chenguang Liu [a,b], Yudan Yuan [f], Xianwei Geng [a,b], Weixuan Li [a], Zhichen Feng [a], Ivona Mitrovic [b], Li Yang [c,d,*], Cezhou Zhao [a,d,*]

[a] Department of Electrical and Electronic Engineering, Xi'an Jiaotong-Liverpool University, Suzhou, Jiangsu 215123, PR China
[b] Department of Electrical Engineering and Electronics, University of Liverpool, Liverpool L69 3GJ, United Kingdom
[c] Department of Chemistry, Xi'an Jiaotong-Liverpool University, Suzhou, Jiangsu 215123, PR China
[d] Department of Chemistry, University of Liverpool, Liverpool L69 7ZD, United Kingdom
[e] School of Intelligent Manufacturing Ecosystem, Xi'an Jiaotong-Liverpool University, Suzhou Jiangsu, 215123, PR China
[f] School of Electronic and Information Engineering, Xi'an Jiaotong University, Xi'an, Shaanxi 710049, PR China

ARTICLE INFO

Article history:
Received 8 October 2020
Received in revised form 6 December 2020
Accepted 11 December 2020
Available online xxx

Keywords
Two-dimensional titanium carbide
Nitrogen doping
Carbon nanotubes
Pseudocapacitances

ABSTRACT

A facile strategy involving only liquid mixing, drying, and annealing processes has been designed to fabricate a new MXene-based material containing nitrogen-doped carbon nanotubes grown on the nitrogen-modified titanium carbides (NCMX). During the thermal treatment, the nitrogen doping is dually achieved in MXene nanosheets and carbon nanotubes while the in-situ growth of carbon nanotubes occurs. The NCMX electrode exhibits the well-designed structure with the promoted specific surface area and specific capacitance. More attractively, the resultant NCMX-4 material shows extraordinary improved electrochemical capacitances of 299.52 F g^{-1} at the scan rate of 2 mV s^{-1} in the 3 M H_2SO_4 electrolyte, which is remarkably more superior than those of the pure un-doped one (74.98 F g^{-1}). It delivers an excellent capacitance retention capability of 84.2% after 10,000 cycles. Our results highlight that the strategy of fabricating novel NCMX materials here can be readily applied to a large industrial scale for improving the pseudocapacitance of supercapacitors.

1. Introduction

With the increasing demands for the electric vehicle industry, supercapacitors (SCs) have been propounded as the latest sort of electrochemical energy storage device. Based on higher capacitances compared with traditional electrostatic capacitors and greater power densities than conventional batteries, the importance of SCs as a candidate for power delivery has been well recognised [1]. Considering the differential charge storage mechanisms, SCs could be divided into electric double-layer capacitors (EDLCs) and pseudocapacitors (PCs) [2]. In EDLCs, the capacitance is generated when the charge physically adsorbs/desorbs at the electrode/electrolyte interface, having a long life time but with limited capacitance. In PCs, the capacitance is produced by highly reversible redox reactions at the interface between electrode and electrolyte, supplying higher energy density but poor stability during the charge and discharge cycles [3,4]. At this instant, most of the commercial products are EDLCs. Still, their specific capacitances are relatively low and cannot meet the growing requirements. Therefore, there are continuous research efforts and technological advances to seek new materials used in SCs with high specific capacitances [2,3].

Two-dimensional (2D) materials are a popular option in the energy storage field. Several key advantages, such as their large specific surface area, active chemical edge sites, high mechanical strength and flexibility, play an essential role and offer the possibility of SCs as next-generation electrochemical devices [5,6]. MXenes, an emerging but quickly augmented group of 2D materials, discovered by Gogotsi's group, have demonstrated enormous potentials and resulted in increased rate capability and cycling stability for the diversified energy storage systems [5]. A general formula to represent MXenes is $M_{n+1}X_nT_x$ (n = 1, 2, or 3). M means an early transition metal. X stands for carbon, nitrogen, or both. T_x illustrates surface functional groups including -O, -OH, and -F. The valence state of Ti, which is connected with the oxygen surface groups, repeatedly changes according to the protonation of oxygen

* Corresponding authors.
E-mail addresses: Li.Yang@xjtlu.edu.cn (L. Yang); Cezhou.Zhao@xjtlu.edu.cn (C. Zhao)

https://doi.org/10.1016/j.jallcom.2020.158347
0925-8388/

functional groups [7,8]. Hence, MXenes show remarkable pseudocapacitive charge storage properties in the acidic electrolyte [9]. However, despite their outstanding features, the collapse of layer-stacking, induced by the strong Van der Waals force between the individual sheet, reduces the surface area to a great extent [10]. This hinders the potential used as electrode materials and further restricts their practical applications for energy storage [11]. Thus, it is essential to evaluate the optimised structure of 2D materials to overcome these defects as much as possible. In recent years, researchers have made many efforts to design the improved structures, for example, integrating it into three-dimensional (3D) structures, amplifying interlayer spacers, and inserting carbon material [12,13]. Gogotsi et al. prepared 3D macroporous MXene frameworks via sacrificial poly(methyl methacrylate) spherical templates, retaining a specific capacitance of 210 F g^{-1} at 10 V s^{-1}. The overall performance had surpassed the best carbon supercapacitors known [14]. Que and his coworkers used urea as intercalant and nitrogen (N) source and constructed 2D N-doped delaminated titanium carbide (N-d-Ti_3C_2), revealing reasonably raised surface area, favourable mesopores, and high conductivity [15]. This N-d-Ti_3C_2 material presented a high specific capacitance of 266.5 F g^{-1} at a scan rate of 5 mV s^{-1}. Wang et al. developed the N-doped $Ti_3C_2T_x$ electrode by post-etch annealing $Ti_3C_2T_x$ in ammonia, exhibiting a 460% increment (192 F g^{-1} in 1 M H_2SO_4) compared to the undoped $Ti_3C_2T_x$ [16]. The improvements of these two studies mainly modified $Ti_3C_2T_x$ in the direction of the increasing interlayer spacing brought from the N-doping, which make the nitrogenous functional groups in the N-doped $Ti_3C_2T_x$ more accessible to the H^+ ion.

Besides the N-doping strategy, introducing one-dimensional nanomaterials, like carbon nanotubes (CNTs) into the MXene-containing composites, also shows great potential in boosting the capacitance performance. Gogotsi et al. also designed flexible, sandwich-like MXene/CNT compound paper electrodes through alternating filtration of MXene and CNT dispersions. A significantly improved gravimetric capacitance of 150 F g^{-1} at 2 mV s^{-1} was achieved with about 30% increment compared with the pure $Ti_3C_2T_x$ [17]. By inserting the CNT into MXene, Xu's group produced the 2D d-Ti_3C_2/CNT mixed electrode with high electrochemical performance (393 F cm^{-1} at 5 mV s^{-1}) and grand rate stability (80% capacitance retention while scan rates increased from 5 to 100 mV s^{-1}) [18]. These two works have provided solid evidence that adding CNTs into MXene could increase the specific capacitance to a large extend.

Driven by these successful studies, it is expected that combining the benefits of N-doping and the addition of CNTs will help address the challenges of MXenes as electrode materials for SCs and further applications in energy storage devices. Herein, the N-doped CNTs@$Ti_3C_2T_x$ (NCMX) composite material was prepared through the facile annealing of the dried starting mixture. During the thermal treatment, the nitrogen is dually doped into $Ti_3C_2T_x$ nanosheets and the in-situ growth of CNTs. By the support of CNTs and doped nitrogen, the structure is improved, and the layer-to-layer re-stacking is largely minimised. The presence of N element in $Ti_3C_2T_x$ and CNTs can provide further negative charges, and additionally supply more pseudocapacitance for specific capacitance. Owing to the collaborative outcome of N-doped CNTs and N-doped $Ti_3C_2T_x$, the supercapacitors with the NCMX under optimised condition display outstanding electrochemical performance of 299.52 F g^{-1} at 2 mV s^{-1}. Compared with the un-doped electrode, this is a remarkably 4-fold improvement. Also, the NCMX-4 electrode delivers a good cycling performance with 84.2% retention after 10,000 cycles. These new results underline that this strategy can be applied to prepare an encouraging pseudocapacitance electrode material for practical applications with great potential in large-scale production.

2. Material and methods

2.1. Preparation of delaminated $Ti_3C_2T_x$ dispersion

The MXene $Ti_3C_2T_x$ was formed by etching Ti_3AlC_2 with the utilisation of lithium fluoride (LiF) and hydrochloric acid (HCl) [19]. Briefly, 2 g of LiF (Aladdin Reagent, Shanghai, China) was dissolved in 40 mL of concentrated HCl (Sinopharm Chemical Reagent, Shanghai, China) with magnetic stirring to make a homogeneous solution. 2 g of Ti_3AlC_2 (Nanjing Dongliang Material Technology Co. Ltd) was mixed in the above solution with stirring, heating at 35 °C for 24 h. The suspension was then collected by centrifugation at a speed of 3500 rpm for 10 min and washed several times with deionised (DI) water until the pH value over 5. Then, the ethanol as the intercalator was introduced into the mixture of the above centrifuge tubes. The resultant solution was performed ultrasonic and centrifugal treatment for several times. The dark green supernatant with fewer stacks was stored in dark glass bottles and reserved under 4 °C. 10 mg mL^{-1} of the as-prepared dispersion of $Ti_3C_2T_x$ was determined by the vacuum filtration of a particular volume of the supernatant, usually, 1 mL.

2.2. Fabrication of NCMX composite material

The nickel acetate tetrahydrate, the dicyandiamide (DICY) and the sucrose were mixed in the 14 mL MXene suspension. The nickel acetate tetrahydrate, the sucrose, and MXene were fixed in a mass ratio of 1:2:4. The DICY was acting as the nitrogen source, and the mass ratio of DICY and $Ti_3C_2T_x$ was varied as 0:1, 2.5:1, 5:1, 10:1, and 20:1. A certain amount of DI water was added to dissolve all the solutes. After 30 min of magnetic stirring, the mixture was dried at 60 °C in a vacuum for 48 h. The dried and rough-ground powder was pre-heated to 600 °C for 2 h, and then the temperature was raised to 800 °C for 2 h with the heating rate of 5 °C min^{-1}. The whole process was conducted under the Ar atmosphere. After being cooled down to the room temperature, the product was taken out and carefully ground to obtain the NCMX composite material. For the simplicity, the samples were denoted as NCMX-1, NCMX-2, NCMX-3, NCMX-4, and NCMX-5, accordingly, in which NCMX-1 represents no addition of DICY and NCMX-5 represents the largest amount of DICY used in the solution.

2.3. Assembly of three-electrode system for supercapacitors

A traditional three-electrode system was adopted to evaluate the electrode material in 3 M H_2SO_4 electrolyte solution, in which the NCMX composite material, the high-purity graphite plate and the Ag/AgCl electrode in saturated potassium chloride (KCl) were served as the working, counter and reference electrodes, respectively. The NCMX powder, carbon black (CB) and polyvinylidene fluoride (PVDF) were mixed in a mass ratio of 8:1:1 and dispersed in the N-methyl pyrrolidone (NMP). Then the homogeneous slurry was coated on a carbon paper (Zhengzhou Jinghong New Energy Technology Co., Ltd) in the required shape of a 1 × 1 cm^2 square and dried-up at 60 °C in a vacuum drying oven to form the final working electrode (the mass of the active material was 3.0–3.5 mg cm^{-2}).

2.4. Construction of two-electrode SSC device

The SSC device was produced in a CR2032 coin cell. A polypropylene paper between two NCMX-4 electrodes in 6 M KOH electrolyte was adopted to be the separator, and the whole mass of electrodes in the SSC device was around 5 mg.

2.5. Materials characterisations

The crystal structures of samples were examined with the X-ray diffraction (XRD, D8 Advance, Bruker, with Cu Kα radiation, λ = 1.5406 Å) analysis. The surface morphology and microstructure of the samples were observed by scanning electron microscopes (SEM, Hitachi SU-8010 and S4700) and transmission electron microscope (TEM, FEI Tecnai G2 F30). Raman spectroscopy investigations were implemented with a laser micro-Raman spectrometer (RENISHAW invia, 532 nm excitation wavelength). Fourier transform infrared spectroscopy (FT-IR, Nicolet iS50, Thermofisher, USA) Through X-ray photoelectron spectroscopy (XPS, ESCALAB 250Xi, Thermo Scientific) with binding energy referenced to the C 1s at 284.6 eV, various chemical bonding states and different surface elemental composition of all as-prepared samples were also identified. The specific surface area was checked using the Brunauere-Emmette-Teller method (BET, Beishide 3H-2000PS2), which utilised N as an adsorbent at liquid nitrogen temperature. All samples were degassed at 60 °C for 3 h before analysis.

2.6. Electrochemical measurements

Electrochemical tests, including cyclic voltammogram (CV) tests, galvanostatic charge-discharge (GCD) cycles, and electrochemical impedance spectroscopy (EIS), were measured in a three-electrode system employing a Metrohm Autolab PGSTAT302N electrochemical workstation at room temperature. CV tests were valued in the potential window of 0–0.6 V at the scan rate from 2 to 200 mV s^{-1}. GCD cycles were carried out at the current density from 1 to 10 A g^{-1}, with the same potential range used for CV tests. EIS was accomplished within a frequency range from 10 to 100 kHz at an open circuit potential of 5 mV. The long-term electrochemical stability was tested at a current density of 5 A g^{-1}. Similar CV, GCD and EIS tests were also conducted for the two-electrode SSC device.

The gravimetric capacitance (C_m, F g^{-1}) was calculated from CV curves through the following equation [20].

$$C_m = \frac{\int_{V_1}^{V_2} IdV}{mv(V_2 - V_1)} \quad (1)$$

where I (A) is the current over the working electrode; V_1 and V_2 (V) represent the upper and lower limit of the potential window, respectively; $V = V_2 - V_1$ (V) is the potential window; m is the mass of the active material in the working electrode; ν (V s^{-1}) represents the scan rate. In this way, V_1, V_2, I, and dV could be calculated from the area of the CV curve.

3. Results and discussions

The synthetic procedure of NCMX composite material can be observed in Scheme 1. Firstly, $Ti_3C_2T_x$ was achieved by etching MAX (Ti_3AlC_2) in the LiF and HCl, and the delaminated $Ti_3C_2T_x$ (d-$Ti_3C_2T_x$) was formed after the centrifugation [19]. Afterwards, the d-$Ti_3C_2T_x$ was mixed with the carbon source, the nitrogen source, and the nickel acetate to create the $Ti_3C_2T_x$-based mixture. Finally, the NCMX samples were achieved via calcining the dried mixture under Ar atmosphere. During the calcination, CNTs were formed by the catalysis of the Ni particles. Simultaneously, when the temperature reached over 200 °C, N functional groups decomposed from the DICY, eventually decorated on the $Ti_3C_2T_x$ and subsequently as-grown CNTs.

The XRD was accomplished to characterise the crystalline structure of NCMX-n (n = 1, 2, 3, 4, 5). Fig. 1 shows that all the samples exhibit similar patterns. For pure $Ti_3C_2T_x$, the diffraction peaks of (002) and (110) planes are located at 6.4° and 61.3°, respectively, which indicate the existence of $Ti_3C_2T_x$ [5,10,21,22]. After DICY-assisted N doping, the characteristic peak of (002) plane of $Ti_3C_2T_x$ is widen and vanishes gradually, probably due to that the transformation of $Ti_3C_2T_x$ was not fully completed and TiN (JCPDS card no. 38–1420) or other amorphous phases were formed [19,20,23,24]. Furthermore, the interlayer spacings of NCMX samples (d-spacing ~ 1.38 nm) are broader than the radius of H^+ (0.12 nm) or K^+ (0.138 nm), which implies that more H^+ or K^+ ions sufficiently react with the materials during the

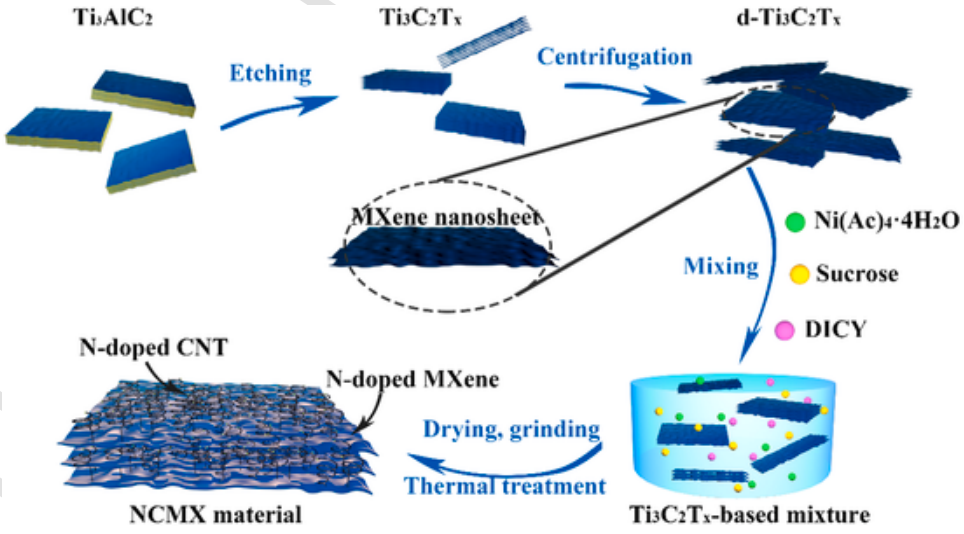

Scheme 1. The schematic of the preparation of NCMX composite material.

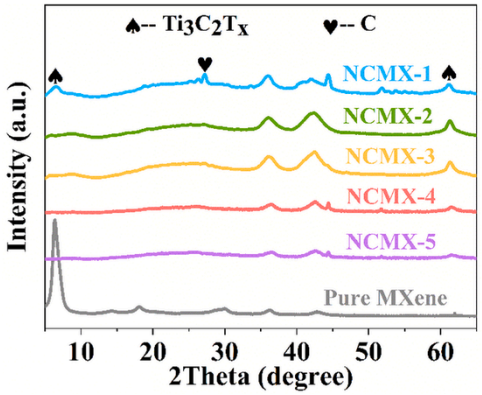

Fig. 1. Materials characterisation of the as-prepared materials: XRD. XRD patterns of NCMX-n (n = 1, 2, 3, 4, 5).

charging-discharging cycles [15,25]. All the samples own the characteristic peak related (002) of carbon, which demonstrates that the CNTs were successfully grown and connected to the MXene nanosheets to form the cross-linked structure.

Field emission SEMs were conducted to evaluate the as-prepared samples' morphology. The SEM image of the NCMX-1 (Fig. 2a) features the well-scattered nanosheets with several straight carbon nanotubes. These dispersed nanosheets imply that the multilayered MXene was delaminated well by ultrasound and centrifugation repeatedly. Furthermore, it is regarded that the CNTs were fabricated by the catalysis of the Ni particles, which own the thin and straight morphology of approximately 25 nm in diameter. Interestingly, the introduction of doped nitrogen appears to have a different effect on the CNTs morphology. Compared to the undoped sample, in Fig. 2b, the CNTs in NCMX-4 present a curving shape and the diameter increase to around 35 nm. The CNTs have two conditions decorating on the $Ti_3C_2T_x$ nanosheets. In Fig. 2c, the CNTs grown on the surface of the individual nanosheet while the CNTs seem to play a role of space-expansion between MXene nanosheets (Fig. 2d). Namely, the addition of the CNTs into the $Ti_3C_2T_x$ can proficiently alleviate the aggregation of individual $Ti_3C_2T_x$ nanosheet and improve the structure to a great extent. Nevertheless, for NCMX-5, the excess nitrogen source brings the damage with some hole and disordered structure on MXene flakes due to the oxidisation effect of CO_2 on $Ti_3C_2T_x$ during the pyrogenic decomposition of the DICY, which can be seen from Fig. S1 [26].

To complete the further investigation of materials in all samples, Raman analysis was performed as displayed in Fig. 3a. The primary influence of several peaks at around 150, 266, 400, and 610 cm^{-1} indicates the Raman vibration for $Ti_3C_2T_x$ [27]. For all the samples, two broad bands are found, both of which are positioned at around 1350 cm^{-1} (D band), and 1585 cm^{-1} (G band). The D band of carbon indicates that the disordered carbon can be confirmed. In contrast, the G band of carbon implies that the existence of graphite lattice with a particular sequence in carbon-based materials. Furthermore, the ratios of peak intensity between D-band and G-band (I_D/I_G) are calculated as 0.66, 0.91, 0.94, 1.02 and 0.96 in samples with NCMX-1, NCMX-2, NCMX-3, NCMX-4, and NCMX-5, re-

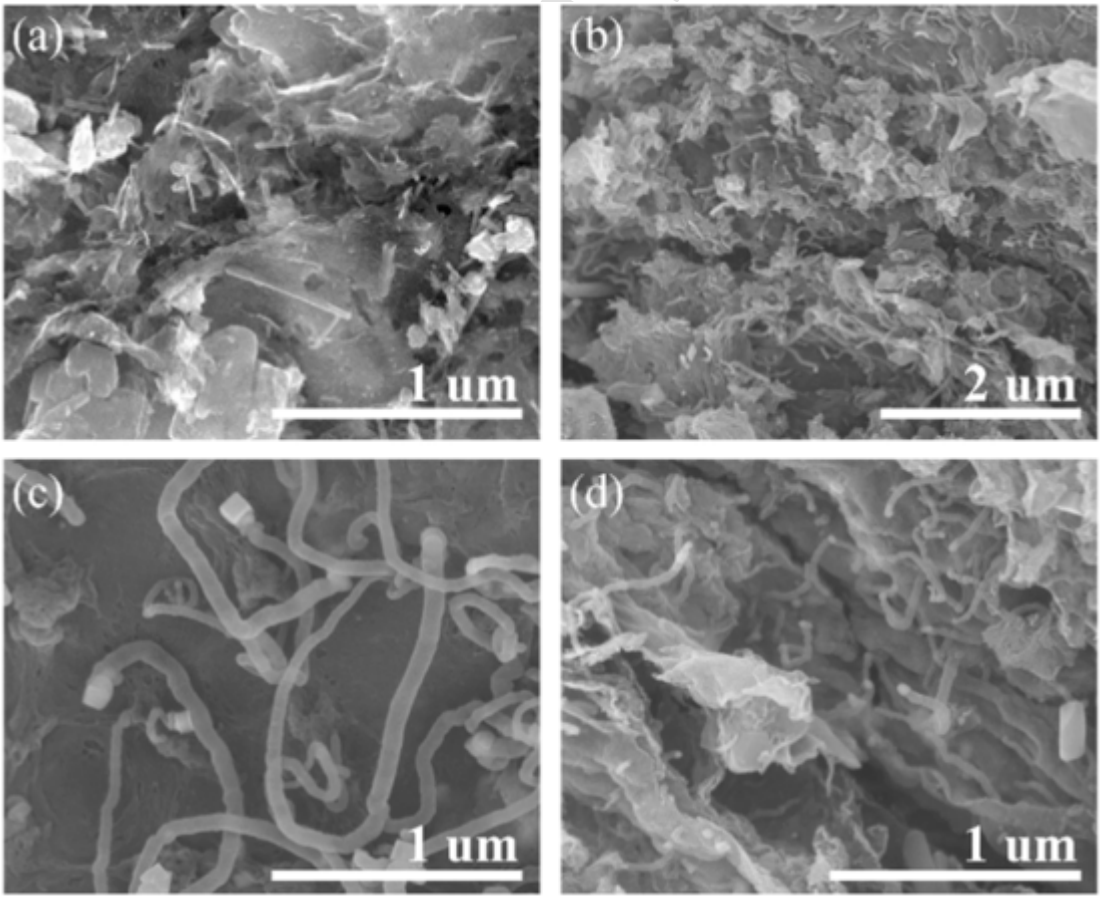

Fig. 2. Materials characterisation of the as-prepared materials: SEM. Low- and high- resolution SEM images of (a) NCMX-1, (b, c, d) NCMX-4.

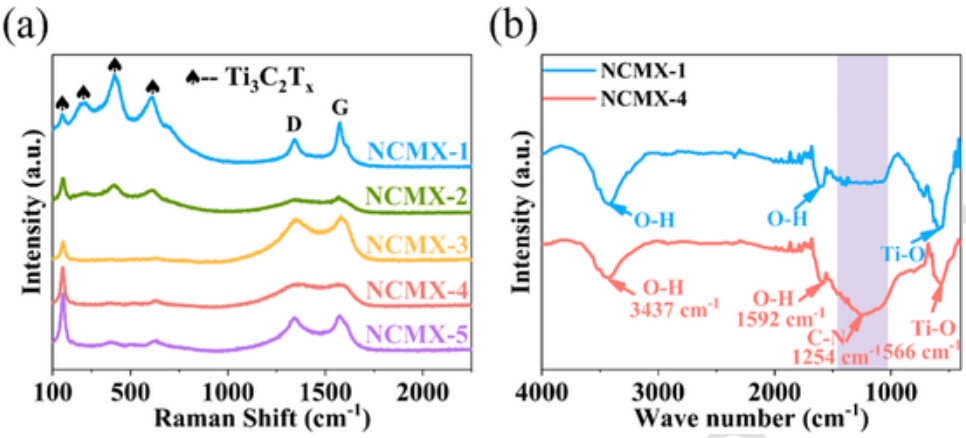

Fig. 3. Materials characterisations of the as-prepared materials: Raman, and FT-IR. (a) Raman spectra of NCMX-n (n = 1, 2, 3, 4, 5), and (b) FT-IR spectra for chemical functionalities of NCMX-1 and NCMX-4.

spectively. Higher I_D/I_G reveals more N defects and CNTs formed in the MXene-based products, resulting in more disordered carbon after calcination. The nitrogen groups existed in the NCMX composite material would effectively add other active sites in favour of the pseudocapacitance.

FT-IR spectra express the chemical functionality of NCMX-1 and NCMX-4, as shown in Fig. 3b. In addition to the coexisted peaks, the peak of ostensible C-N of the NCMX-4 sample is observed at ~ 1254 cm^{-1} while no similar peak exists in NCMX-1. This means that the nitrogen was doped into the CNTs and $Ti_3C_2T_x$ nanosheets concurrently during the simple thermal treatment. Extra nitrogen functional groups would make for the increased pseudocapacitive properties [15,16,20,28,29].

The microstructure of NCMX-4 heterostructure was further examined by using the TEM. Fig. 4a-c display the structure of MXene sheets. In the high-resolution TEM (HRTEM), the 0.22 nm and 0.26 nm d-spacings agree with the (200) and (111) lattice fringes of MXene layers, respectively. From Fig. 4d-f, the morphology of CNTs is evident with the distinct bamboo joints, which is inconsistent with the SEM results. Nitrogen doping would produce a signature and unique morphology of CNTs [30,31]. The bamboo joint is a seal formed by a fullerene-like structure, which is caused by the five-membered ring of graphite produced by the doping of nitrogen. Calculations show that nitrogen atoms tend to form five-membered rings when forming covalent bonds with carbon atoms, which reduces the system energy by 71.4 kJ mol^{-1} [31]. When the five-membered ring contains two nitrogen atoms, it can even reduce the system energy by 97.0 kJ mol^{-1}. The introduction of the five-membered ring makes the six-membered ring network plane appear to be twisted, thereby forming a seal of the fullerene-like structure, such as the bamboo. In Fig. 4f, the

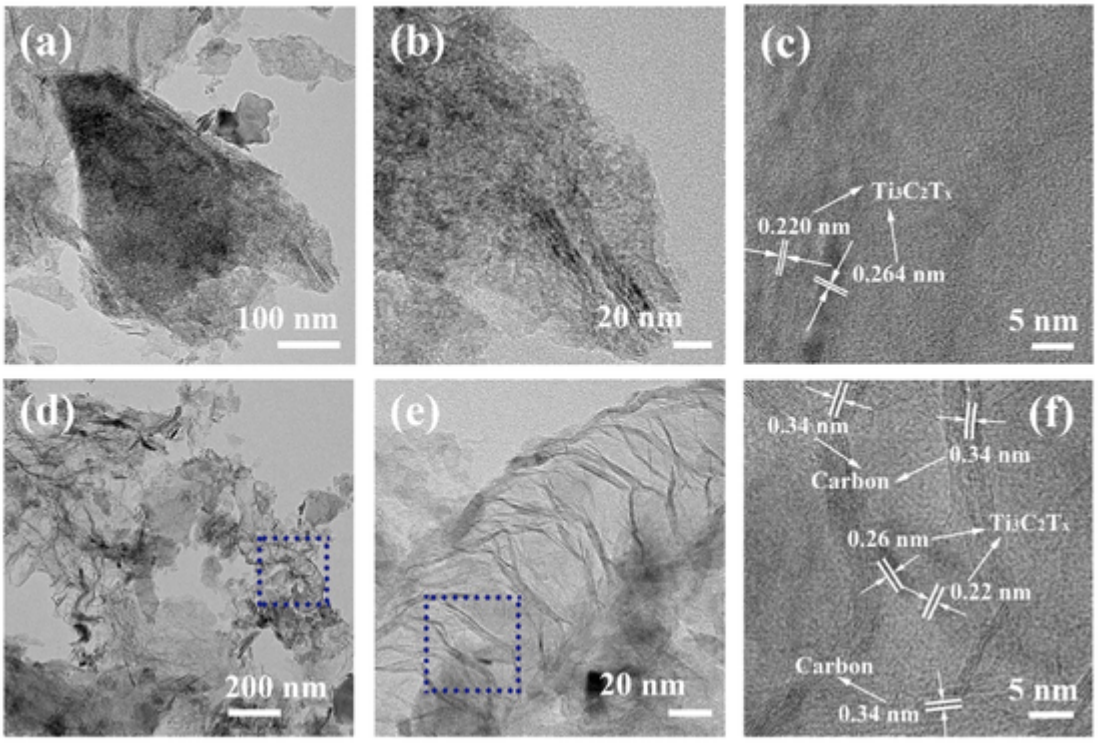

Fig. 4. Materials characterisation of the as-prepared materials: TEM. (a-f) Low- and high- resolution TEM images of NCMX-4 samples.

0.34 nm d-spacing matches the (002) lattice fringes of graphitic carbon, while the 0.26 nm d-spacing is regarded as the MXene layers, which shows that scattered MXene sheets are attached to the tube wall of the CNTs. Moreover, EDS was carried out to probe further the existence of doped-N in MXene nanosheets (Fig. S2). N element is observed with its distribution on the sheets, confirming the successful N-doping on the $Ti_3C_2T_x$. Also, abundant -O (or -F) element associated with the etching process is also found while almost no Al element is observed, supporting the SEM results. Hence, it is expected that the NCMX materials may serve as an optimal architecture with the uniformly doped-nitrogen and the efficient avoidance of $Ti_3C_2T_x$ re-stacking with the support of CNTs.

The composition of elements and chemical bonding states in NCMX were measured by XPS. Fig. 5a illustrates the XPS survey spectrum of NCMX-1 and NCMX-4 materials, where the signal matchings of the O 1*s* and F 1*s* are discovered along with those of Ti 2*p* and C 1*s* for Ti_3AlC_2. Also, the Al 2*p* signal has not been detected on these two samples, suggesting the absolute removal of Al by HF. Besides, the NCMX-4 presents a new signal of N 1*s* at about 400 eV after the thermal treatment with DICY, revealing the N element's existence. Table 1 indicates that the contents of various elements have been measured using the XPS spectrum. The C element content in N- NCMX-4 is quite higher than NCMX-1, which is probably attributed to the N-doped thickened CNTs formed during the cal-

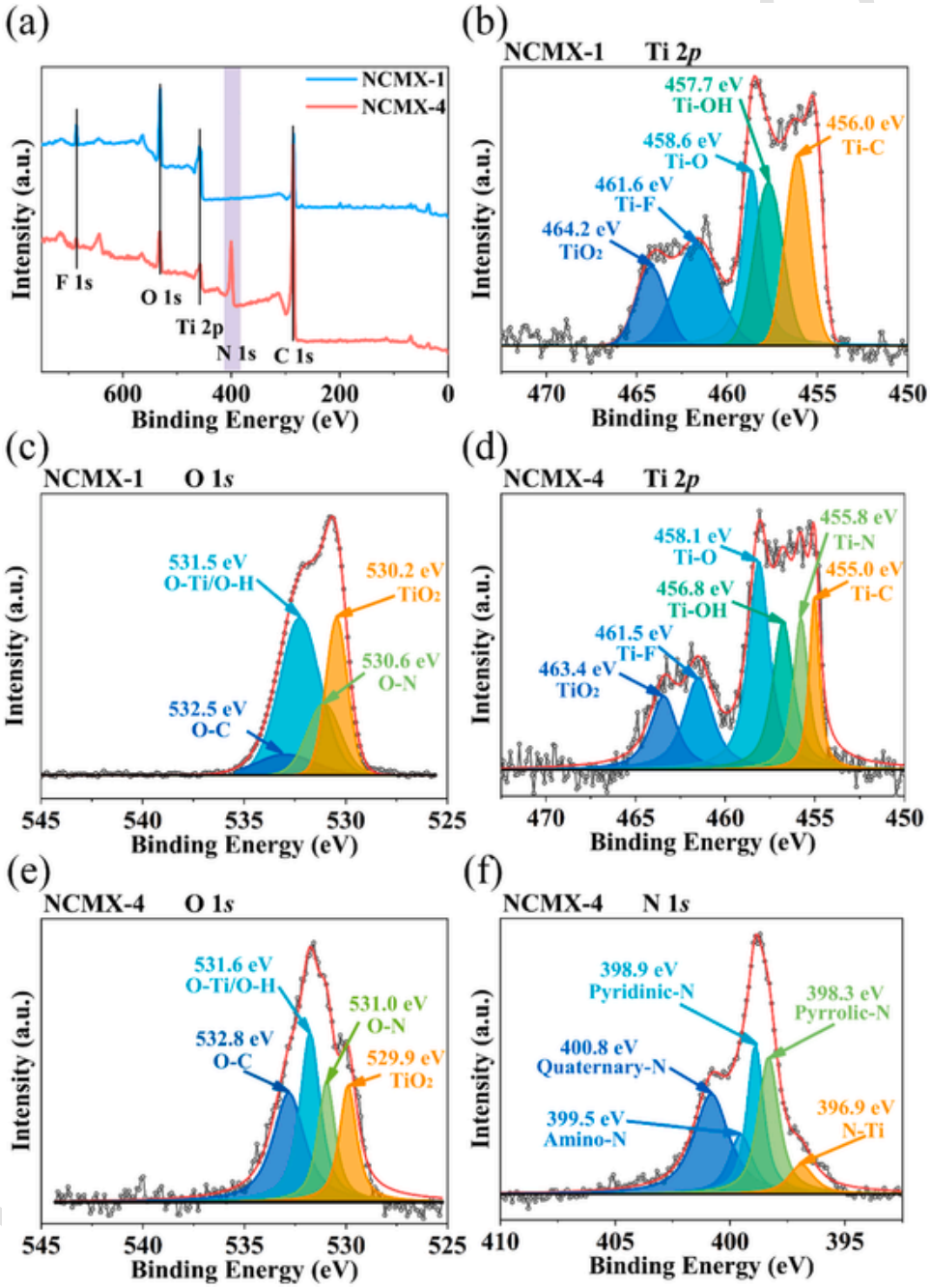

Fig. 5. Materials characterisation of the as-prepared materials: XPS. (a) XPS survey spectra of NCMX-1 and NCMX-4 samples. The high-resolution XPS spectra of NCMX-1 material: (b)Ti 2*p*, (c) O 1*s*. The high-resolution XPS spectra of NCMX-4 material: (d)Ti 2*p*, (e) O 1*s*, (f) N 1*s*.

Table 1
The composition of various elements in NCMX-1 and NCMX-4 calculated by XPS.

Samples	NCMX-1	NCMX-4
Ti (At%)	11.91	2.66
C (At%)	54.94	68.98
O (At%)	25.26	6.98
N (At%)	0.49	17.21
F (At%)	4.37	1.68
Ni (At%)	3.02	2.49

cination. The high-resolution XPS spectra in the Ti 2*p* region of NCMX-1 (Fig. 5b) and NCMX-4 (Fig. 5d) could extract into six-type prominent component peaks, in agreement with Ti—C, Ti—N, Ti—O, Ti—OH, Ti—F, and TiO_2 at their corresponding binding energies, accordingly [32,33]. Here, the Ti-N shown in NCMX-4 reveals that the nitrogen of DICY interacts with Ti to form Ti—N covalent bonds during the calcination. The O 1*s* spectrum of NCMX-4 (Fig. 5e) indicates four peaks accorded to TiO_2, O—N, O—Ti/O—H, and O—C at 529.9 eV, 531.0 eV, 531.6 eV, and 532.8 eV, respectively [25,33]. Fascinating, compared with the O 1 *s* spectrum of NCMX-1 (Fig. 5c), the O—C and O—N peaks of NCMX-4 are increased dramatically, which means that the nitrogen is efficiently doped into $Ti_3C_2T_x$ and the carbon nanotubes are connected to the MXene nanosheets. Five-type major component peaks are available for the high-resolution N 1 *s* core-level spectra: N—Ti bond at 396.9 eV, pyrrolic-N at 398.3 eV, pyridinic-N at 398.9 eV, amino-N at 399.5 eV, and quaternary-N at 400.8 eV (Fig. 5f) [16,20,33]. The C 1*s* peaks at 284.6 eV, 285.4 eV, 286.4 eV and 289.3 eV are ascribed to the characteristic bonds of C—C, C—N, C—H, and C—F, respectively (Fig. S3) [34]. The F 1*s* spectrum (Fig. S4) demonstrates three peaks centred at 684.4 eV, 685.2 eV and 685.9 eV from the F—Ti, F—Ni and F—C bonds, accordingly [16]. These XPS outcomes prove that the carbon nanotubes are in-situ grown successfully and the N atoms of DICY has been decomposed and doped into CNTs and MXene nanosheets during the thermal treatment.

Surface area measurements were further applied to explore the NCMX composite by the nitrogen adsorption and desorption (Fig. 6a-b). Type IV isotherms with distinct hysteresis loops in the range of 0.45–1.0 P/P_0 are presented for all samples, revealing the appearance of a mesoporous construction. By the BET method, shown in Table 2, the specific surface areas of NCMX-2, NCMX-3, NCMX-4, and NCMX-5 are calculated to be 66.20, 96.22, 112.01 and 154.82 $m^2\ g^{-1}$, accordingly, which is much larger than NCMX-1 (46.97 $m^2\ g^{-1}$). The enhanced specific surface area may offer three benefits: (i) the larger diameter of N-doped CNTs, (ii) the alleviation of $Ti_3C_2T_x$ re-stacking by CNTs, (iii) more activate sites relevant to the nitrogen functional group. As shown in Fig. 5b and Table 2, as calculated by Barret-Joyner-Halenda (BJH) method, NCMX-1, NCMX-2, NCMX-3, and NCMX-4 have a narrow pore-size distribution centred at approximately 2.95, 2.41, 2.54, and 2.28 nm, respectively, compared with NCMX-5 (9.73 nm). The improved specific surface area and optimal pore size distribution are beneficial for exposing active sites and readily transporting ions, consequently leading to an increased electrochemical performance of the N-doped materials.

Electrochemical performances, containing CV tests, GCD cycles, and EIS of NCMX-n (n = 1, 2, 3, 4, 5) electrodes, were tested by the three-electrode system. Owing to its outstanding ionic conductivity and tiny protons, the acidic electrolyte, 3 M H_2SO_4, was selected in favour of the pseudocapacitance. CV curves of various samples can be observed in Fig. 7a. All samples were measured with the scan rate of 20 mV s^{-1} and the potential range of 0–0.6 V. Capacitances can be easily compared by means of the area of the CV curve vividly. The NCMX-1 has a small rectangular curve, resulting in a low capacitance. By comparison, the NCMX-2, 3, 4, 5 exhibit superb capacitive performances with the relatively larger areas, due to the extra redox pseudocapacitive effects linked with N. Nevertheless, NCMX-2, 3, 4, 5 display the semi-rectangular shape, caused by the fast electro-adsorption and intercalation/de-intercalation of H^+, which take place on or near the surface of the active electrode materials. The intercalation/de-intercalation processes of the cations (H^+) are derived from these two reactions:

$$N - Ti_3C_2 + xH^+ + xe^- \leftrightarrow H_xN - Ti_3C_2 \quad (2)$$

$$Ti_3C_2O_y + yH^+ + ye^- \leftrightarrow Ti_3C_2O_yH_y \quad (3)$$

where N represents -NH_2 and -NO_2 for NCMX samples [25,35,36].

Fig. 7b reveals CV curves of the NCMX-4 electrode at scan rates of 2, 5, 10, 20, 50, 100, and 200 mV s^{-1}. Even with a high scan rate of 200 mV s^{-1}, the CV curves of the NCMX-4 electrode still maintain similar shapes, showing the excellent rate property and low internal resistance [37]. After calculation, in Fig. 7c, the NCMX-4 electrode delivers the highest specific capacitance of 299.52 F g^{-1} at 2 mV s^{-1}, compared with the NCMX-1 electrode (74.98 F g^{-1}), NCMX-2 electrode (79.95 F g^{-1}) and NCMX-3 electrode (157.87 F g^{-1}), NCMX-5 electrode (186.10 F g^{-1}). Notably, among these five different ratios of DICY to MXene, the NCMX-4 electrode owns the opti-

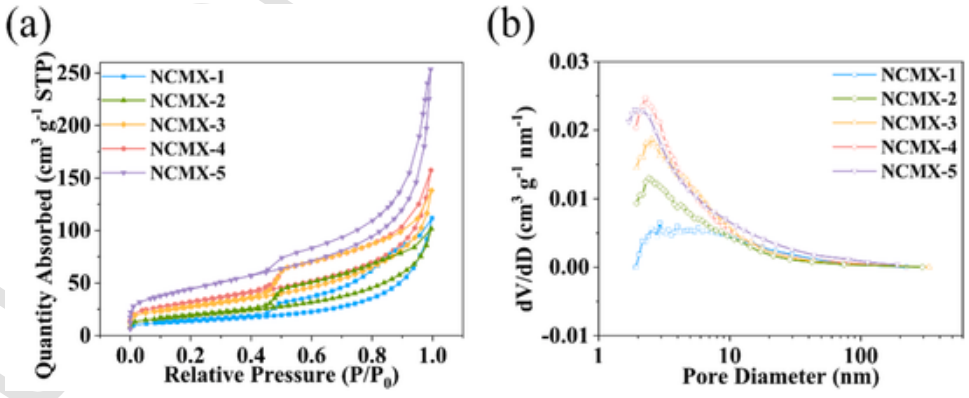

Fig. 6. Materials characterisation of the as-prepared materials: BET. (a) Nitrogen adsorption-desorption isotherms, and (b) pore size distribution calculated from N_2 desorption isothermals for NCMX-n (n = 1, 2, 3, 4, 5) samples.

Table 2
The specific surface area and pore-size distribution calculated from the BET method.

NCMX-n (n = 1, 2, 3, 4, 5)	1	2	3	4	5
Specific surface area ($m^2\ g^{-1}$)	46.97	66.20	96.23	112.01	154.82
Pore-size distribution (nm)	2.95	2.41	2.54	2.28	9.73

mal N amount. In addition, the NCMX-4 electrode exhibits excellent rate capability with 48.13% capacitance retention as the scanning rate upgrading from 5 mV s^{-1} to 200 mV s^{-1}.

Fig. 7d displays the GCD curves in 3 M H_2SO_4 at 2 A g^{-1}. All the charge-discharge curves are closely triangular. The internal resistance could be achieved at the beginning of discharge curves. Compared with the discharging period of other NCMX materials, the NCMX-4 is surprisingly longer, illustrating that the NCMX-4 supports a higher capacitance, which is compatible with the CV curves. Fig. 7e shows the GCD curves of NCMX-4 under different current densities from 1 A g^{-1} to 10 A g^{-1}. The triangular-shape curves of GCD exhibit highly-alterable performance, which reflects the as-fabricated electrode samples own remarkable electrochemical reversibility and rapid I-V response.

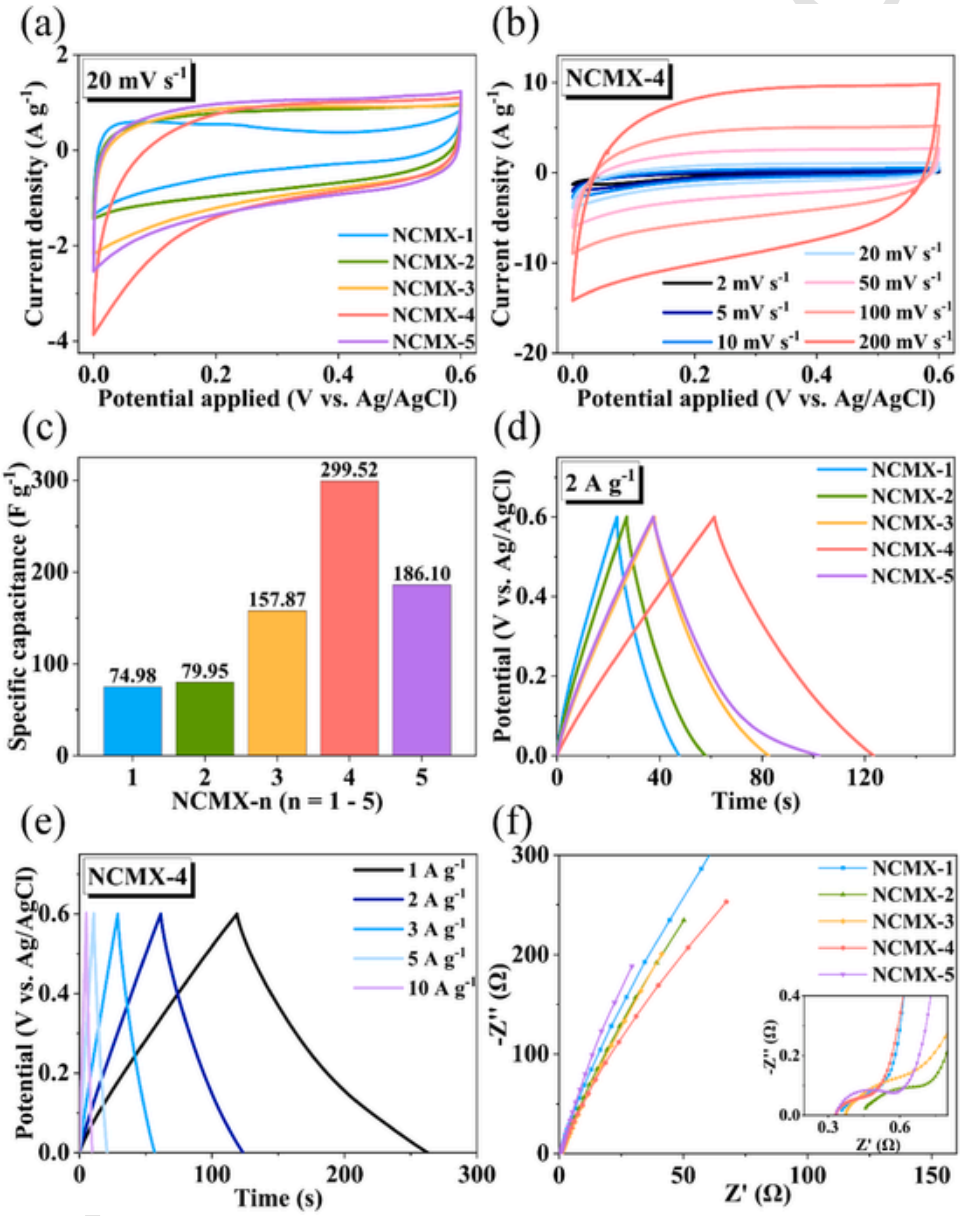

Fig. 7. Electrochemical properties of the devices with the three-electrode configuration in 3 M H_2SO_4 solution. (a) CV curves of all samples with the scan rate at 20 mV s^{-1}. (b) CV curves of the NCMX-4 electrodes at scan rates from 2 to 200 mV s^{-1}, respectively. (c) Specific capacitances of the NCMX-n (n = 1–5) electrodes at the scan rate of 2 mV s^{-1}. (d) GCD curves at the current density of 2 A g^{-1}. (e) GCD of the NCMX-4 electrodes at current densities from 1 to 5 A g^{-1}. (f) Impedance Nyquist plots of all the samples with frequency in a range from 10 mHz to 100 kHz. The inserts are the magnification in the high-frequency region.

EIS was utilised to analyse the electrochemical system further. Fig. 7f depicts the Nyquist plots (100 kHz - 10 mHz) with inserts showing the magnification in the high-frequency region. Generally, the diameter of the semicircular arc and the charge transfer resistance (R_{ct}) are highly connected because of ions transferring across the whole interface between the accessible area of the electrode material and the electrolyte [8]. With the increases of the electroactive surface area and electrical conductivity of the electrode material, a lower R_{ct} is obtained. The intricate and rough microstructure of NCMX-2, 3, 4, 5 samples can facilitate charge transfer of cations, and therefore, the high electroactive surface area can be generated. While simulating the EIS spectra of Nyquist plot of the NCMX electrodes, the equivalent electrical circuits were adopted, and each component in them was computed (Fig. S5 and Table S1). With the best response, the NCMX-4 ($R_s = 0.32\,\Omega$) electrode show the lowest internal resistance in comparison with the NCMX-1 ($R_s = 0.35\,\Omega$), NCMX-2 ($R_s = 0.42\,\Omega$), NCMX-3 ($R_s = 0.37\,\Omega$), and NCMX-5 ($R_s = 0.33\,\Omega$). In addition, the NCMX-4 ($R_{ct} = 0.21\,\Omega$) electrode owns the smallest charge transfer resistance in contrast with the NCMX-1 ($R_{ct} = 0.25\,\Omega$), NCMX-2 ($R_{ct} = 0.41\,\Omega$), NCMX-3 ($R_{ct} = 0.38\,\Omega$), and NCMX-5 ($R_{ct} = 0.27\,\Omega$). This fast frequency response of NCMX-4 is caused by the proper amount of the nitrogen species. Therefore, the nitrogen doping in NCMX-4 promotes the electrolyte ion transmission rate in the supercapacitor.

Symmetrical SCs (SSCs) were fabricated to access the practical application of the NCMX-4 material. The NCMX-4//NCMX-4 SSC device was assembled in a stainless steel CR2032 coin cell with 6 M KOH electrolyte. CV curves of the SSC device at different potential ranges with the scan rate of $10\,mV\,s^{-1}$ can be observed in Fig. 8a. When the voltage windows are 0–1.0 V or lower, there is no visible polarisation phenomenon occurring in the approximately rectangular-shape CV curves. Therefore, the SSC device can operate in the voltage window of 0–1.0 V. At various scan rates and with 0–1.0 V potential range, the SSC device with the rectangular-shape CV scanning curves displays relatively enhanced capacitive behaviour, excellent rate characteristic and better reversibility (Fig. 8b). GCD curves of the SSC device in Fig. 8c were obtained under different current densities within 0–1.0 V, which indicates a triangular shape of the SSC device with the high current density at $5\,A\,g^{-1}$. The Nyquist plot in Fig. 8d provides further verification of the low internal resistance and excellent capacitive behaviour of the NCMX-4 electrode.

Fig. 9 displays GCD cycling curves of the NCMX-4 electrode at a current density of $5\,A\,g^{-1}$, evaluating long-term electrochemical stability of the electrode. The capacitance retention of the NCMX-4 electrode remains around 84.2% after 10,000 cycles, indicating excellent long-term durability. Hence, it can be concluded that the NCMX-4 electrode is promising for electrical storage application.

Based on the above results, coupled with the recent studies on nitrogen-doping or metal-containing CNTs for electrochemical storage devices [15–18,20,25,28,29,38–41], the increased electrochemical properties of the NCMX-4 electrode can be ascribed to the rationally designed structure in these parts. (i) The N-doped MXene nanosheets with the increased spacing can accelerate charge transfer and promote the stability of the mixture. Simultaneously, the doped nitrogen helps the 2D morphology overcome the re-stacking, compress the path for electron transport and H^+ diffusion, and offer high

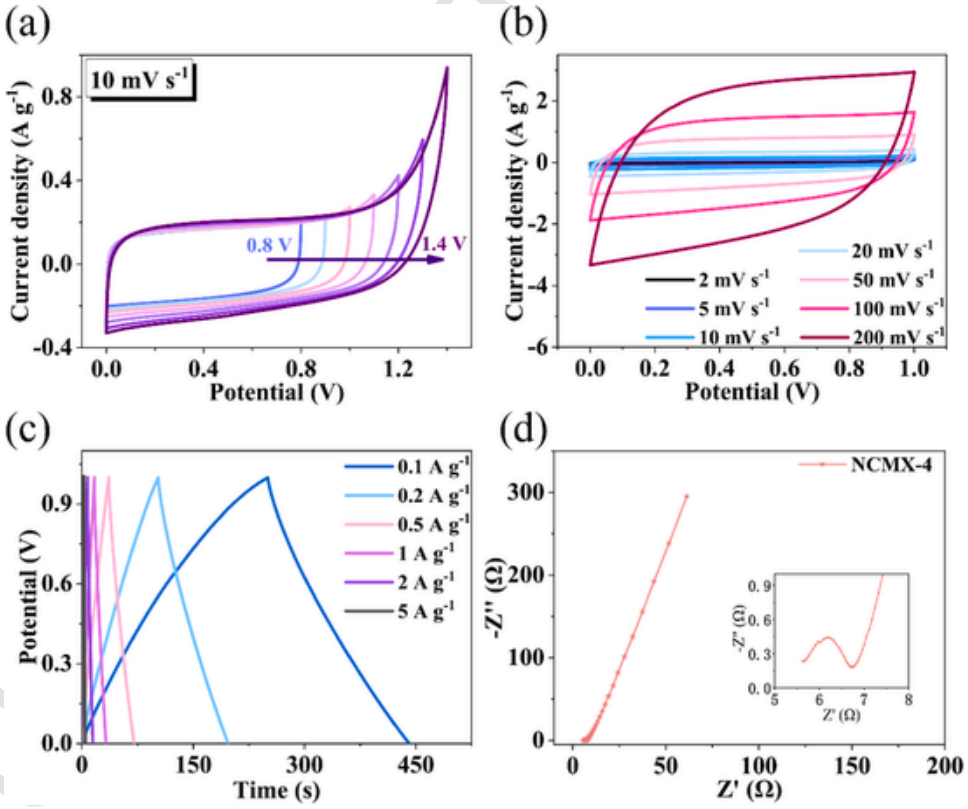

Fig. 8. Electrochemical performance of the NCMX-4//NCMX-4 SSC device in 6 M KOH. (a) CV curves in different potential ranges at the scan rate of $10\,mV\,s^{-1}$. (b) CV curves in the voltage window of 0–1.0 V at from 2 to $200\,mV\,s^{-1}$. (c) GCD curves at current densities from 0.1 to $5\,A\,g^{-1}$. (d) Impedance Nyquist plots of the NCMX-4//NCMX-4 SSC device. The insert is the magnified curves in the high-frequency region.

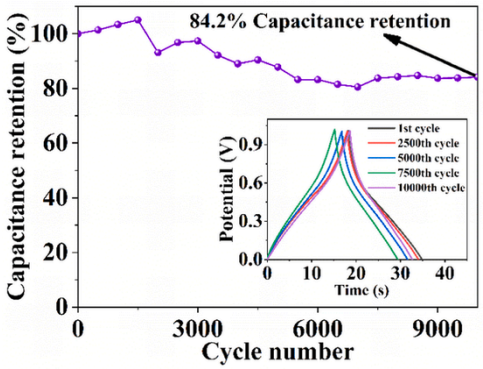

Fig. 9. Electrochemical performance of the devices with the three-electrode configuration in 3 M H_2SO_4 solution. Capacitance retention of the NCMX-4 electrode (10,000 GCD cycles) at 5 A g^{-1}, with the insert showing GCD curves of the NCMX-4 electrode after the first, 2500th, 5000th,7500th, and 10,000th cycle.

rate performance. (ii) In-situ growth of N-doped CNTs, not only increases the conductivity of the whole electrode but also virtually enlarges the specific surface area, which provides abundant electroactive sites in favour of electrolyte diffusion. (iii) In the self-assembled composites, all N-doped $Ti_3C_2T_x$ nanosheets and CNTs are electrically conducting and mutually support each other to fabricate the cross-linked skeleton that is advantageous both in-plane (with MXene nanosheets) and off-plane (amongst nanosheets) transmission of electrons. Besides, the re-stacking of $Ti_3C_2T_x$ nanosheets can be further impeded by N-doped CNTs as layer-layer spacers, supporting multidimensional ion diffusion pathways. Owing to the above features, the superior electron conductivity and facile ion diffusion pathways are concurrently achieved, offering enhanced electrochemical properties of the NCMX-4 electrode.

4. Conclusions

To sum up, novel nitrogen-doped CNTs@$Ti_3C_2T_x$ has been successfully constructed by a simple heat treatment method. Herein, DICY and sucrose play significant roles during the synthesis process of the NCMX material, serving as the nitrogen source for doping functionalisation and carbon source for CNTs catalysed by Ni particles. On the grounds of the collective function of the 2D structure, in-situ grown CNTs and suitable N doping amount, the NCMX-4 electrode displays a high specific capacitance of 299.52 F g^{-1} at a scan rate of 2 mV s^{-1} in 3 M H_2SO_4 electrolyte, which is almost four times of that of the un-doped electrode. It delivers superior cycling stability of 84.2% capacitance retention after 10,000 cycles at 5 A g^{-1} in 3 M H_2SO_4 electrolyte. This simple synthesis method can be adopted to other MXene-based materials and used as promising pseudocapacitance electrode materials for practical applications.

CRediT authorship contribution statement

Yi Sun: Conceptualization, Methodology, Validation, Investigation, Data curation, Writing - original draft, Visualization. **Ruowei Yi:** Methodology, Validation. **Yinchao Zhao:** Resources. **Chenguang Liu:** Software. **Yudan Yuan:** Conceptualization. **Xianwei Geng:** Resources. **Weixuan Li:** Investigation, Writing - review & editing. **Zhichen Feng:** Formal analysis. **Ivona Mitrovic:** Supervision. **Li Yang:** Writing - review & editing, Supervision, Funding acquisition. **Cezhou Zhao:** Supervision, Funding acquisition.

Declaration of Competing Interest

The authors declare that they have no known competing financial interests or personal relationships that could have appeared to influence the work reported in this paper.

Acknowledgments

This work was supported by the National Natural Science Foundation of China (NSFC Grants 21750110441), State Key Laboratory of Materials Processing and Die and Mould Technology, Huazhong University of Science and Technology (P2019-019), Suzhou Industrial Park Initiative Platform Development for Suzhou Municipal Key Lab for New Energy Technology (RR0140), the Key Program Special Fund in XJTLU (KSF-A-04, KSF-E-28, KSF-E-38).

Declaration of competing interests

The authors declare that they have no known competing financial interests or personal relationships that could have appeared to influence the work reported in this paper.

Appendix A. Supporting information

Supplementary data associated with this article can be found in the online version at doi:10.1016/j.jallcom.2020.158347.

References

[1] A. Gonzalez, E. Goikolea, J. Andoni Barrena, R. Mysyk, Review on supercapacitors: technologies and materials, Renew. Sustain. Energy Rev. 58 (2016) 1189–1206.
[2] M. Salanne, B. Rotenberg, K. Naoi, K. Kaneko, P.L. Taberna, C.P. Grey, B. Dunn, P. Simon, Efficient storage mechanisms for building better supercapacitors, Nat. Energy 1 (2016) 16070.
[3] C. Choi, D.S. Ashby, D.M. Butts, R.H. DeBlock, Q. Wei, J. Lau, B. Dunn, Achieving high energy density and high power density with pseudocapacitive materials, Nat. Rev. Mater. 5 (2019) 5–19.
[4] S. Fleischmann, J.B. Mitchell, R. Wang, C. Zhan, D.E. Jiang, V. Presser, V. Augustyn, Pseudocapacitance: from fundamental understanding to high power energy storage materials, Chem. Rev. 120 (2020) 6738–6782.
[5] M. Naguib, O. Mashtalir, J. Carle, V. Presser, J. Lu, L. Hultman, Y. Gogotsi, M.W. Barsoum, Two-dimensional transition metal carbides, ACS Nano 6 (2012) 1322–1331.
[6] C. Zhan, M. Naguib, M. Lukatskaya, P.R.C. Kent, Y. Gogotsi, D.-e Jiang, Understanding the MXene pseudocapacitance, J. Phys. Chem. Lett. 9 (2018) 1223–1228.
[7] C. Zhang, Y. Ma, X. Zhang, S. Abdolhosseinzadeh, H. Sheng, W. Lan, A. Pakdel, J. Heier, F. Nüesch, Two-dimensional transition metal carbides and nitrides (MXenes): synthesis, properties, and electrochemical energy storage applications, Energy Environ. Mater. 3 (2020) 29–55.
[8] M. Hu, Z. Li, T. Hu, S. Zhu, C. Zhang, X. Wang, High-capacitance mechanism for $Ti_3C_2T_x$ MXene by in situ electrochemical Raman spectroscopy investigation, ACS Nano 10 (2016) 11344–11350.
[9] X. Mu, D. Wang, F. Du, G. Chen, C. Wang, Y. Wei, Y. Gogotsi, Y. Gao, Y. Dall'Agnese, Revealing the pseudo-intercalation charge storage mechanism of MXenes in acidic electrolyte, Adv. Funct. Mater. 29 (2019) 1902953.
[10] P. Simon, Two-dimensional MXene with controlled interlayer spacing for electrochemical energy storage, ACS Nano 11 (2017) 2393–2396.
[11] C. Liu, Z. Yu, D. Neff, A. Zhamu, B.Z. Jang, Graphene-based supercapacitor with an ultrahigh energy density, Nano Lett. 10 (2010) 4863–4868.
[12] K. Li, M.Y. Liang, H. Wang, X.H. Wang, Y.S. Huang, J. Coelho, S. Pinilla, Y.L. Zhang, F.W. Qi, V. Nicolosi, Y.X.

Xu, 3D MXene architectures for efficient energy storage and conversion, Adv. Funct. Mater. (2020).
[13] G. Tontini, M. Greaves, S. Ghosh, V. Bayram, S. Barg, MXene-based 3D porous macrostructures for electrochemical energy storage, J. Phys. Mater. 3 (2020) 022001.
[14] M.R. Lukatskaya, S. Kota, Z. Lin, M.-Q. Zhao, N. Shpigel, M.D. Levi, J. Halim, P.-L. Taberna, M.W. Barsoum, P. Simon, Y. Gogotsi, Ultra-high-rate pseudocapacitive energy storage in two-dimensional transition metal carbides, Nat. Energy 2 (2017) 17105.
[15] C. Yang, Y. Tang, Y. Tian, Y. Luo, M. Faraz Ud Din, X. Yin, W. Que, Flexible nitrogen-doped 2D titanium carbides (MXene) films constructed by an ex situ solvothermal method with extraordinary volumetric capacitance, Adv. Energy Mater. 8 (2018) 1802087.
[16] T. Zhao, J. Zhang, Z. Du, Y. Liu, G. Zhou, J. Wang, Dopamine-derived N-doped carbon decorated titanium carbide composite for enhanced supercapacitive performance, Electrochim. Acta 254 (2017) 308–319.
[17] X. Xie, M.-Q. Zhao, B. Anasori, K. Maleski, C.E. Ren, J. Li, B.W. Byles, E. Pomerantseva, G. Wang, Y. Gogotsi, Porous heterostructured MXene/carbon nanotube composite paper with high volumetric capacity for sodium-based energy storage devices, Nano Energy 26 (2016) 513–523.
[18] P. Yan, R. Zhang, J. Jia, C. Wu, A. Zhou, J. Xu, X. Zhang, Enhanced supercapacitive performance of delaminated two-dimensional titanium carbide/carbon nanotube composites in alkaline electrolyte, J. Power Sources 284 (2015) 38–43.
[19] M. Ghidiu, M.R. Lukatskaya, M.Q. Zhao, Y. Gogotsi, M.W. Barsoum, Conductive two-dimensional titanium carbide 'clay' with high volumetric capacitance, Nature 516 (2014) 78–81.
[20] Y. Wen, T.E. Rufford, X. Chen, N. Li, M. Lyu, L. Dai, L. Wang, Nitrogen-doped $Ti_3C_2T_x$ MXene electrodes for high-performance supercapacitors, Nano Energy 38 (2017) 368–376.
[21] Y. Cai, J. Shen, G. Ge, Y. Zhang, W. Jin, W. Huang, J. Shao, J. Yang, X. Dong, Stretchable $Ti_3C_2T_x$ MXene/carbon nanotube composite based strain sensor with ultrahigh sensitivity and tunable sensing range, ACS Nano 12 (2018) 56–62.
[22] F. Zhang, X. Guo, P. Xiong, J. Zhang, J. Song, K. Yan, X. Gao, H. Liu, G. Wang, Materials for energy, Adv. Energy Mater. 10 (2020).
[23] O. Mashtalir, M. Naguib, B. Dyatkin, Y. Gogotsi, M.W. Barsoum, Kinetics of aluminum extraction from Ti_3AlC_2 in hydrofluoric acid, Mater. Chem. Phys. 139 (2013) 147–152.
[24] J. Luo, X. Tao, J. Zhang, Y. Xia, H. Huang, L. Zhang, Y. Gan, C. Liang, W. Zhang, Sn^{4+} ion decorated highly conductive Ti_3C_2 MXene: promising lithium-ion anodes with enhanced volumetric capacity and cyclic performance, ACS Nano 10 (2016) 2491–2499.
[25] C. Yang, W. Que, X. Yin, Y. Tian, Y. Yang, M. Que, Improved capacitance of nitrogen-doped delaminated two-dimensional titanium carbide by urea-assisted synthesis, Electrochim. Acta 225 (2017) 416–424.
[26] C.J. Zhang, S. Pinilla, N. McEvoy, C.P. Cullen, B. Anasori, E. Long, S.-H. Park, A. Seral-Ascaso, A. Shmeliov, D. Krishnan, C. Morant, X. Liu, G.S. Duesberg, Y. Gogotsi, V. Nicolosi, Oxidation stability of colloidal two-dimensional titanium carbides (MXenes), Chem. Mater. 29 (2017) 4848–4856.
[27] Z. Pan, X. Ji, Facile synthesis of nitrogen and oxygen co-doped C@Ti_3C_2 MXene for high performance symmetric supercapacitors, J. Power Sources 439 (2019) 1–10.
[28] Y. Yoon, M. Lee, S.K. Kim, G. Bae, W. Song, S. Myung, J. Lim, S.S. Lee, T. Zyung, K.S. An, A strategy for synthesis of carbon nitride induced chemically doped 2D MXene for high-performance supercapacitor electrodes, Adv. Energy Mater. 8 (2018) 1703173.
[29] Y. Tian, W. Que, Y. Luo, C. Yang, X. Yin, L.B. Kong, Surface nitrogen-modified 2D titanium carbide (MXene) with high energy density for aqueous supercapacitor applications, J. Mater. Chem. A 7 (2019) 5416–5425.
[30] Y. Liu, H. Jiang, Y. Zhu, X. Yang, C. Li, Transition metals (Fe, Co, and Ni) encapsulated in nitrogen-doped carbon nanotubes as bi-functional catalysts for oxygen electrode reactions, J. Mater. Chem. A 4 (2016) 1694–1701.
[31] H. Sjostrom, S. Stafstrom, M. Boman, J. Sundgren, Superhard and elastic carbon nitride thin films having fullerenelike microstructure, Phys. Rev. Lett. 75 (1995) 1336–1339.
[32] J. Wang, D.N. Tafen, J.P. Lewis, Z. Hong, A. Manivannan, M. Zhi, M. Li, N. Wu, Origin of photocatalytic activity of nitrogen-doped TiO_2 nanobelts, J. Am. Chem. Soc. 131 (2009) 12290–12297.
[33] M. Sathish, B. Viswanathan, R.P. Viswanath, C.S. Gopinath, Synthesis, characterization, electronic structure, and photocatalytic activity of nitrogen-doped TiO_2 nanocatalyst, Chem. Mater. 17 (2005) 6349–6353.
[34] L. Shen, X. Zhou, X. Zhang, Y. Zhang, Y. Liu, W. Wang, W. Si, X. Dong, Carbon-intercalated $Ti_3C_2T_x$ MXene for high-performance electrochemical energy storage, J. Mater. Chem. A 6 (2018) 23513–23520.
[35] Q. Tang, Z. Zhou, P. Shen, Are MXenes promising anode materials for Li ion batteries? computational studies on electronic properties and Li storage capability of Ti_3C_2 and $Ti_3C_2X_2$ (X = F, OH) monolayer, J. Am. Chem. Soc. 134 (2012) 16909–16916.
[36] S.-Y. Lin, X. Zhang, Two-dimensional titanium carbide electrode with large mass loading for supercapacitor, J. Power Sources 294 (2015) 354–359.
[37] Q. Zhao, Q. Zhu, J. Miao, P. Zhang, P. Wan, L. He, B. Xu, Flexible 3D porous MXene foam for high-performance lithium-ion batteries, Small 15 (2019) 1904293.
[38] X. Liang, Y. Rangom, C.Y. Kwok, Q. Pang, L.F. Nazar, Interwoven MXene nanosheet/carbon-Nanotube composites as Li-S cathode hosts, Adv. Mater. 29 (2017) 1603040.
[39] W. Zheng, P. Zhang, J. Chen, W.B. Tian, Y.M. Zhang, Z.M. Sun, In situ synthesis of CNTs@Ti_3C_2 hybrid structures by microwave irradiation for high-performance anodes in lithium ion batteries, J. Mater. Chem. A 6 (2018) 3543–3551.
[40] J. Wang, T. Zhao, Z. Yang, Y. Chen, Y. Liu, J. Wang, P. Zhai, W. Wu, MXene-based Co, N-codoped porous carbon nanosheets regulating polysulfides for high-performance lithium-sulfur batteries, ACS Appl. Mater. Interfaces 11 (2019) 38654–38662.
[41] G. Jiang, N. Zheng, X. Chen, G. Ding, Y. Li, F. Sun, Y. Li, In-situ decoration of MOF-derived carbon on nitrogen-doped ultrathin MXene nanosheets to multifunctionalize separators for stable Li-S batteries, Chem. Eng. J. 373 (2019) 1309–1318.